PLANT SCIENCES

Cell wall–derived mechanical signals control cell growth and division during root development

Noemi Svolacchia[1], Marco Marconi[2], Julian Elijah Politsch[2], Federico Vinciarelli[1], Michela De Nittis[1], Elena Salvi[3], Mariana Sotelo-Silveira[4], Alessio Terenzi[3], Gaia Bertolotti[1], Claudia Testi[5], Giancarlo Ruocco[5,6], Raffaele Dello Ioio[1], Riccardo Di Mambro[3], Paolo Costantino[1], Krzysztof Wabnik[2,7]*, Sabrina Sabatini[1]*

Organogenesis emerges from the interplay between genetic and physical interactions within a growing cellular system. While numerous studies have explored how genetic and molecular networks regulate cell activity, the impact of physical interactions and the resulting mechanical constraints on organ development remains poorly understood. In this study, we combine extensive genetic analysis, live imaging, and mechanical measurements with spatiotemporal computational modeling to show that, in the *Arabidopsis* root, changes in the mechanical properties of elongating cell walls influence growth and division rate of neighboring meristematic cells, thereby shaping root development. We propose that the cell wall serves as a crucial source of both autonomous and non-autonomous mechanical signals, providing a compelling example of how mechanical forces contribute to organ growth and development.

INTRODUCTION

Plant and animal morphogenesis differ in that plant cells do not migrate to reach their final functional position. Instead, because of the presence of a semirigid cell wall, plant cells are positioned through specific sequences of cell division events where the spatial disposition of daughter cells is fixed. The final shape of tissues and organs is determined by the combined patterns of cell division, cell expansion, and cell differentiation. These fundamental biological processes are not only genetically regulated but are also influenced by mechanical interactions between cells. While the genetic components involved in these processes are increasingly well characterized, relatively little is known about how the physical interactions between cells and the resulting mechanical constraints contribute to organ development in space and time.

The root of *Arabidopsis thaliana* serves as an ideal system for integrating genetic and biophysical studies, due to its relatively simple and clearly organized structure. In this system, within a tissue, cell division, cell elongation, and cell differentiation are coordinated in time and space, allowing every differentiated cell to be traced back to a single stem cell (*1*).

The *Arabidopsis* root is radially organized in concentric tissue layers, with the lateral root cap and the epidermis as the outermost tissues and the vascular bundle at the center. Along the longitudinal axis, the mature root consists of distinct domains of cellular activity: the stem cell niche, from which all root tissues originate; the division zone (meristem), where the stem progeny cells actively divide; the elongation zone (EZ), where cells cease division and begin to expand and differentiate; and the differentiation zone, where cells complete their elongation and acquire their final size and specialized characteristics, based on their respective tissue types (Fig. 1A). In each tissue layer, the boundary separating meristematic cells from elongating cells is referred to as the transition boundary (TB). Since the TB position varies across tissues, the area encompassing all these boundaries is collectively known as the transition zone (TZ) (Fig. 1A) (*2*, *3*).

A dynamic equilibrium between cell division in the stem cell niche and in the meristem, as well as cell differentiation in the elongation/differentiation zone, ensures a stable population of meristematic cells. This balance maintains the position of the TZ and supports indeterminate root growth (*2*–*4*).

In previous works, we combined molecular genetics with computational modeling to identify minimal molecular networks that dynamically regulate the position of the TZ, root meristem expansion, and the overall rate of root growth (*5*). These networks hinge on the mutual inhibition of key plant hormones such as auxin and cytokinin and the activity of transcription factors like PLETHORAs and ARABIDOPSIS RESPONSE REGULATORs. This interplay is essential for defining and maintaining the boundaries between cell division and differentiation activities (*5*–*8*). In addition to hormones and transcription factors, changes in the cell wall composition and its mechanical properties also play an essential role during root morphogenesis (*9*–*15*). Despite growing evidence that mechanical forces shape plant development, how they mechanistically regulate root morphogenesis is still poorly understood.

To address this gap, we used the pectin methyltransferase gene *QUASIMODO2* (*QUA2*) as a genetic and biophysical tool to modify cell wall composition and mechanical properties in a zone-specific manner. By integrating developmental genetics, biomechanics, and computer simulations of root growth, we provide evidence that modulating the cell wall mechanical properties of elongating cells imposes growth constraints on meristem cells, influencing their division

[1]Department of Biology and Biotechnology "Charles Darwin," University of Rome "La Sapienza," via dei Sardi, 70, 00185 Rome, Italy. [2]Centro de Biotecnología y Genómica de Plantas (CBGP, UPM-INIA) Universidad Politécnica de Madrid (UPM)–Instituto Nacional de Investigación y Tecnología Agraria y Alimentaria (INIA, CSIC), Campus de Montegancedo, Pozuelo de Alarcón, 28223, Madrid, Spain. [3]Department of Biology, University of Pisa, via L. Ghini, 13, 56126 Pisa, Italy. [4]Laboratorio de Bioquímica, Departamento de Biología Vegetal, Facultad de Agronomía, Universidad de la República, Avenida Garzón 780, Montevideo, CP 12900, Uruguay. [5]Center for Life Nano- and Neuro-Science, Istituto Italiano di Tecnologia, Viale Regina Elena 291, 00161 Roma, Italy. [6]Dipartimento di Fisica, Università di Roma "Sapienza," I-00185, Rome, Italy. [7]Departamento de Biotecnología-Biología Vegetal, Escuela Técnica Superior de Ingeniería Agronómica, Alimentaria y de Biosistemas, Universidad Politécnica de Madrid (UPM), Madrid, 28040, Spain.
*Corresponding author. Email: k.wabnik@upm.es (K.W.); sabrina.sabatini@uniroma1.it (S.S.)

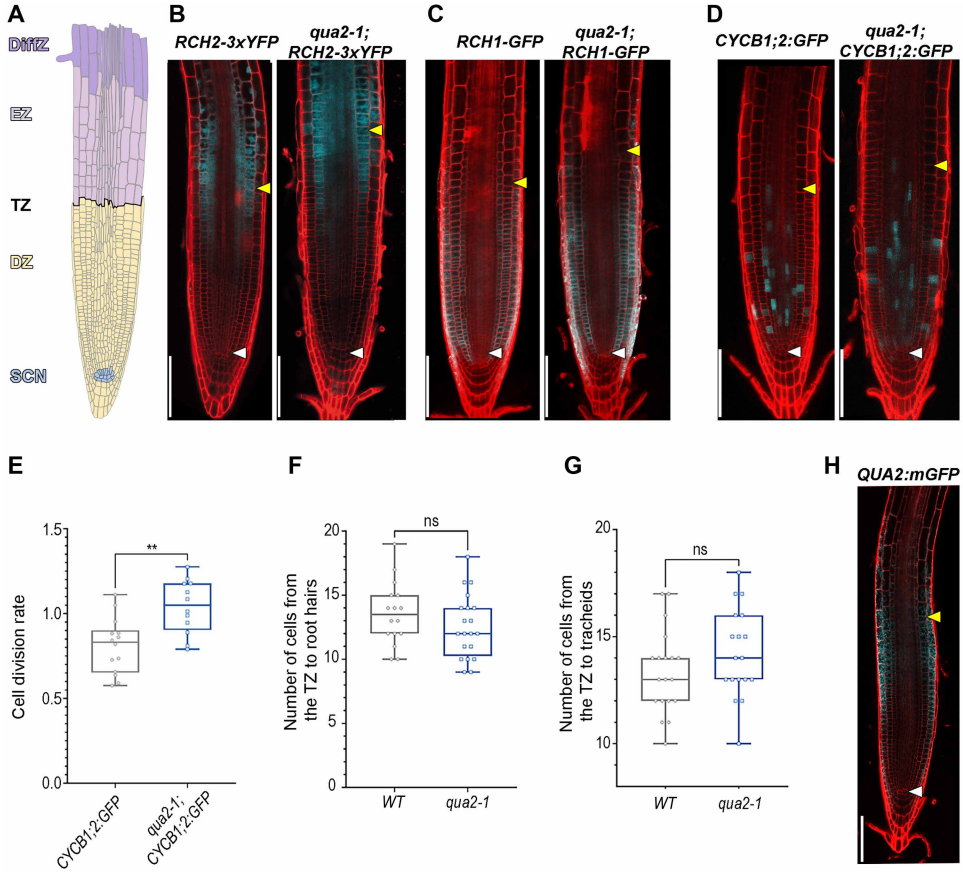

Fig. 1. QUA2-dependent changes in cell wall composition affect cell division. (**A**) Schematic representation of *A. thaliana* mature root zones. SCN, stem cell niche; DZ, division zone; DiffZ, differentiation zone. (**B**) Confocal images of root meristems highlighting the expression of the TZ marker line, *RCH2-3xYFP* in WT and in *qua2-1* mutant roots. (**C**) Confocal images of root meristems highlighting the expression of the meristem marker line, *RCH1-GFP* in WT and in *qua2-1* mutant roots. (**D**) Confocal images of root meristem highlighting the expression of the *CYCB1;2:GFP* marking actively dividing cells in WT and in *qua2-1* mutant roots. (**E**) Cell division rate of WT and *qua2-1* plants. $^{**}P \leq 0.01$, unpaired Student's *t* test. $n = 14$ and 12, $N = 3$. (**F**) Number of cortex cells from the TZ to the first root hair of WT and of *qua2-1* mutant roots. not significant (ns), unpaired *t* test. $n = 16$ and 20, $N = 3$. (**G**) Number of cortex cells from the TZ to the first tracheid of WT and in *qua2-1* mutant roots. not significant (ns), unpaired *t* test. $n = 19$ and 18, $N = 3$. (**H**) Confocal image of root meristem highlighting the expression of the *QUA2:mGFP* translational fusion construct. In all pictures, yellow arrowheads and white arrowheads indicate the TZ and the quiescent center (QC), respectively. Scale bars, 100 μm.

activity. This mechano-biochemical regulation determines the position of the TZ and the size of the meristem and governs the overall rate of root organ growth and development.

RESULTS

QUA2-dependent changes in cell wall composition affect cell division

The primary cell wall is a complex structure composed of a network of cellulose microfibrils, hemicellulose, and a highly cross-linked matrix of pectin polysaccharides (*16*). Few studies have suggested that changes in cell wall composition can influence primary root development (*9*–*12*, *15*). We decided to further corroborate these findings by analyzing the root meristem phenotypes of various mutants with known alterations in the primary cell wall structure. Specifically, we examined the cellulose synthase CESA3 mutant [*isoxaben resistant1-2* (*ixr1-2*)], which has been shown to exhibit reduced cellulose microfibril crystallinity (*17*); the *murus4-2* (*mur4-2*) allele, which disrupts *MURUS4* (*MUR4*), a UDP-D-xylose 4-epimerase required for L-arabinose synthesis leading to a reduction in cell wall arabinose content; two *GALACTURONOSYLTRANSFERASE10* (*GAUT10*) mutant alleles [*galacturonosyltransferase10-2* (*gaut10-2*) and *gaut10-3*], implicated in pectin biosynthesis and associated with decreased levels of galacturonic acid and xylose (*12*, *15*, *18*); and the *quasimodo2-1* (*qua2-1*) mutant, which affects the *QUA2*gene, a pectin methyltransferase known to cause reductions in both pectin content and crystalline cellulose resulting in cell adhesion defects (*19*, *20*). In these mutants, the positioning of the TZ, and thus meristem size, was altered corroborating the notion that changes in the cell wall composition modulate root development (fig. S1, A to F) (*11*, *12*, *15*, *18*).

A possible explanation of how these changes in cell wall composition impinge on root development is that these modifications alter cell wall mechanical properties, and this affects cell behavior and ultimately root development. To verify this hypothesis and to provide a proof of concept, we focused on the *QUA2* gene as the *qua2-1* mutant exhibits a clear root phenotype characterized by a long meristem but a shorter root with a reduced growth rate than wild-type (WT) plants (Fig. 1, B and C, and fig. S1, E to I). This phenotype was confirmed by an additional mutant allele, *qua2-5*, that we generated by CRISPR-Cas9 technology (fig. S1, J to M). To determine whether

the changes in meristem size observed in the *qua2-1* mutant involve alterations in cell division and/or cell differentiation activities, we used several division and differentiation markers.

Analysis of the *ROOT CLAVATA HOMOLOG2-3xYFP* (*RCH2-3xYFP*) marker line, which identifies the position of the TZ (*4*), revealed that in *qua2-1* loss-of-function mutants, the TZ is shifted upward (Fig. 1B). In addition, the expression domains of the *RCH1-GFP* marker line, which highlight the division zone (*4*), was broader in *qua2-1* mutants compared to WT plants (Fig. 1C). These observations align with the enlarged meristem phenotype of the *qua2-1* mutants. To further investigate the cell division activity in *qua2-1*, we measured the cell division rate index in the proximal meristem using the *CYCLIN B1;2:GFP* (*CYCB1;2:GFP*) reporter (Fig. 1, D and E) (*21*). Results showed a higher division rate in the *qua2-1* mutants, indicating that QUA2 acts as a suppressor of cell division (Fig. 1, D and E). This conclusion was further supported by the analysis of the *CYCB1;1:GUS* marker line (*6*), which highlight actively dividing cells throughout the meristem, and by quantitative reverse transcription polymerase chain reaction (RT-qPCR) analysis, which showed elevated expression levels of positive cell cycle regulators such as *CYCB1;1* and *CYCD3;1* in the *qua2-1* mutant (fig. S1, N and O). Conversely, the expression of *CYCLIN-DEPENDENT KINASE INHIBITOR2* (*KRP2*), a negative regulator of cell cycle progression, was reduced (fig. S1O).

Last, we analyzed the position (number of cells from the TZ) of cell differentiation markers, such as the vascular xylem elements and root hairs. All these analyses revealed that the position of root hairs and xylem elements did not change in the *qua2-1* mutants, suggesting that QUA2 does not interfere with cell differentiation (Fig. 1, F and G).

On the basis of these findings, we concluded that QUA2-dependent changes in cell wall composition modulate cell cycle progression, thus controlling TZ position and therefore root meristem size and root growth. QUA2, to control meristem size, acts through a mechanism independent of the known cytokinin pathway (*4*–*7*, *9*), as the mutant remains sensitive to treatments with this hormone (fig. S1P).

We then explored the expression and localization pattern of the QUA2 protein. We generated plants carrying a translational fusion of the QUA2 protein to GFP, under the control of the *QUA2* promoter (*pQUA2-mGFP-gQUA2, QUA2:mGFP* plants). The QUA2 protein is expressed throughout the root but with higher levels in the epidermis at the TZ (Fig. 1H and fig. S1, Q and R).

Cell wall softening controls meristem size

We next investigated whether QUA2-dependent effects on cell wall composition (reductions in both pectin content and crystalline cellulose) (*19*, *20*) might bear on the mechanical properties of the cell wall, using atomic force microscopy (AFM). We focused on epidermal cells at the TZ, where the QUA2 protein is primarily expressed. As shown in Fig. 2A, the Young's modulus indicates that epidermal *qua2-1* cell walls at the TZ are stiffer than the cell walls of WT plants [see also fig. S2 (A and B)].

These results were further and independently confirmed with Brillouin microscopy, a label-free, optical technique that measures the longitudinal modulus at high frequencies. This modulus relates

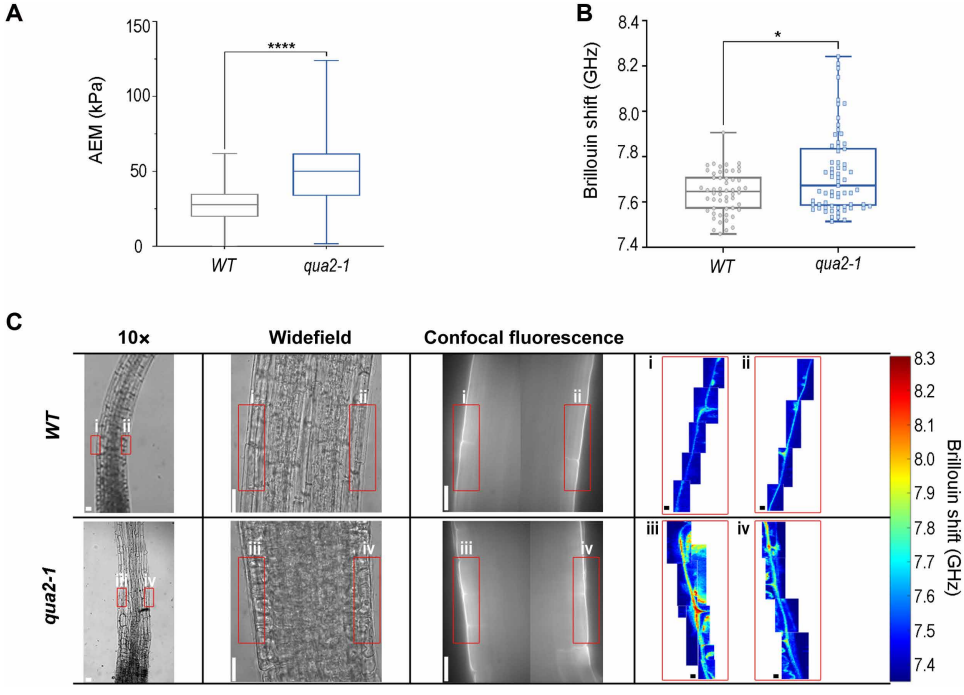

Fig. 2. Cell wall loosening controls meristem size. (**A**) The box plot representing the apparent Young's modulus (AEM) from WT (five seedlings, 2710 force curves, 27.86 ± 10.69 kPa) and *qua2-1* roots (eight seedlings, 1957 force curves, 48.07 ± 21.41 kPa) showing that the apparent elastic modulus of the *qua2-1* mutant is 72.5% higher than WT roots. ****$P \leq 0.0001$, Mann-Whitney *U* test. (**B**) Brillouin shifts relative to Brillouin microscopy maps shown in (C). The cell wall of the *qua2-1* mutant has significantly higher Brillouin shift than WT. *$P \leq 0.05$, Mann-Whitney *U* test. $n = 54$ and 65 cell walls taken from at least 10 independent plants. (**C**) Representative bright-field (shown both at 10× and at 60×), confocal fluorescence (calcofluor white signal from the cell walls), and Brillouin shift maps of WT and a *qua2-1* mutant cell wall of differentiated epidermal cells. Scale bars, 20 μm.

uniaxial stress to uniaxial strain and reflects the material's response under volume changes, thus differing from the quasi-static Young's modulus measured by AFM which does not involve any volume change. Recent reviews have highlighted the Brillouin shift as a robust indicator of the mechanical properties of biological samples (*22*–*25*), and multiple influential studies have successfully applied this method to *A. thaliana* have been proven to be reliable indicators of stiffness. Figure 2B shows Brillouin maps of WT and *qua2-1* roots. These maps were complemented with simultaneous confocal spinning-disk acquisitions of roots labeled with calcofluor white: Using these fluorescent signals as binary masks for region of interest selection, we quantified the mechanical properties of the cell wall specifically, revealing significantly higher Brillouin shifts and thus higher stiffness, in *qua2-1* cell walls compared to WT roots (Fig. 2, B and C). Therefore, these results provide a further confirmation that alterations in the cell wall composition of the *qua2-1* mutant lead to a stiffer epidermal cell wall compared to the WT, suggesting that the QUA2 protein activity promotes cell wall softening, which in turn influences cell division, meristem size, and root growth.

Cell wall softening of elongating cells limits cell division of meristematic cells

To investigate how QUA2-dependent cell wall softening influences cell cycle activity, meristem size, and root growth, we built a computer model to explore plausible scenarios in which QUA2 reduces cell wall stiffness. The root growth model builds on a mechano-biochemical framework recently developed that integrates key processes, including cell division, elongation, and growth biomechanics (*26*). In our model, cells within the lateral root cap (meristem) divide once they have doubled in size, whereas cells in the TZ—defined shootward from the last lateral root cap cell—expand in response to uniform internal turgor pressure. By coupling cell wall relaxation with growth-induced deformation, the model allows testing how changes in the cell wall mechanical property (i.e., softening) affects individual cells and their neighbors.

Since QUA2 is predominantly expressed in the epidermis at the TZ, with lower levels in other root tissues (Fig. 1H and fig. S1P), we preserved this pattern in our simulations by linking QUA2 expression to cell wall relaxation (WT-like) (Fig. 3A). To simulate the *qua2-1* mutant, we reduced QUA2 expression to negligible levels (qua2-like) (Fig. 3B). These simulations predicted an enlarged meristem and a reduced root growth rate compared to the "WT-like" simulation, as also observed in the in vivo *qua2-1* mutant (fig. S1, E, F, and I, and movie S1, A and B). Thus, the model predictions support in vivo observations, indicating that QUA2-dependent cell wall softening would influence the position of the TZ and thereby regulate root and root meristem size. The model predicts that it is sufficient to express QUA2 specifically at the TZ to limit meristem size and increase root growth (Fig. 3, C to E, and movie S1C).

To test these predictions in vivo, we manipulated QUA2 expression using both complementation and overexpression approaches. In the *qua2-1* mutant background, QUA2 was reintroduced at the TZ using a dexamethasone (Dex)–inducible system under the RCH2 promoter [*qua2-1*;*pRCH2-GVG-ter-6xUAS-mCITRINE-gQUA2*, *RCH2>>gQUA2* (*qua2-1*) plants]. In these plants, Dex treatment was sufficient to rescue root growth and the enlarged root meristem and to decrease cell cycle progression of meristematic cells, as indicated by RT-qPCR analysis of *CYCB1;1*, *CYCD3;1*, and *KRP2* genes (Fig. 3, F and G, and fig. S3, A and B). At the same time, overexpressing QUA2 at the TZ in WT plants using the same construct (*RCH2>>gQUA2*) led to reduced meristem size and increased root length upon Dex treatment, resembling model predictions (Fig. 3, C to E, H, and I, and fig. S3C). AFM measurements confirmed increased elasticity of the elongating epidermal cell walls in QUA2-overexpressing roots (Fig. 3J and fig. S3, D and E). Moreover, CRISPR-based tissue-specific knockout (CRISPR-TSKO) experiments (*27*), where the *QUA2* gene was specifically mutated only at the TZ by expressing *Cas9* under the *RCH2* promoter (*RCH2:Cas9-GFP-sgQUA2* plants), reproduced the *qua2-1* mutants meristem (Fig. 3, K and L). In contrast, expressing QUA2 in the meristem [*qua2-1; pRCH1-GVG-ter-6xUAS-mCITRINE-gQUA2* plants, *RCH1>>gQUA2* (*qua2-1*)] did not rescue the *qua2-1* phenotype underling the critical and spatially restricted role of QUA2 activity at the TZ (Fig. 3, M and N, and fig. S3F). Together, these data suggest that QUA2-dependent softening of cell walls at the TZ (i.e., alteration of the mechanical properties) restricts cell division in the meristem, thus shaping root meristem size and root growth.

Mechanical constraints generated by elongating cells control cell division in the meristem

Next, we set out to understand how changes in the mechanical properties of the cell wall at the TZ control the cell division activity of the neighboring meristematic cells. Model simulations of WT-like, qua2-like mutants and QUA2-TZ roots predict that changes in meristem size are accompanied by dynamic changes in cell deformation (i.e., the capacity of the cells to elongate and change their shape) and root growth (Fig. 4, A and B, and movie S2). In simulations of the qua2-like mutant, the increase in meristem size results from reduced cell deformation and overall growth in the TZ zone, coupled to enhanced cell deformation and growth in the meristem compared to the WT-like simulation (Fig. 4, A and B). In these simulations, epidermal and cortical elongating cells are relatively smaller and shorter than those of WT-like simulations (fig. S4A). At the contrary, in simulations of QUA2-TZ, cells in the TZ elongate faster leading to higher deformation rates coupled to reduced cell deformation and growth in the meristem compared to the WT-like simulation (Fig. 4, A and B, and fig. S4A). As the model links cell wall mechanics with growth-induced stress transmission between connected cells, it predicts that meristem size is dynamically regulated and inversely related to the mechanical constraints exerted by elongating cells on dividing cells. In qua2-like, a stiffer cell wall restricts cell deformation of elongating cells, resulting in weaker mechanical constraints on dividing cells, prompting cell division and leading to an enlarged meristem. Conversely, in the QUA2-TZ, a softer cell wall enhances cell deformation of elongating cells that generate stronger mechanical constraints on actively dividing cells inhibiting cell division thus leading to a shorter meristem.

Direct detection of mechanical constraints in living organisms remains extremely challenging, as they are neither visible nor readily measurable. Therefore, to further validate our hypothesis, we next analyzed the consequences of these constrains on cell size and cell growth dynamics.

We analyzed the final size of differentiated epidermal and cortical cells in plants with different meristem lengths. Plants with a long meristem included *qua2-1* mutants and plants where QUA2 is disrupted only in the TZ (*pRCH2:Cas9-GFP-sgQUA2*). Plants with a reduced meristem included WT plants overexpressing QUA2 (*RCH2>>gQUA2*) and *qua2-1* plants in which QUA2 activity was specifically rescued at the TZ [*RCH2>>gQUA2* (*qua2-1*)].

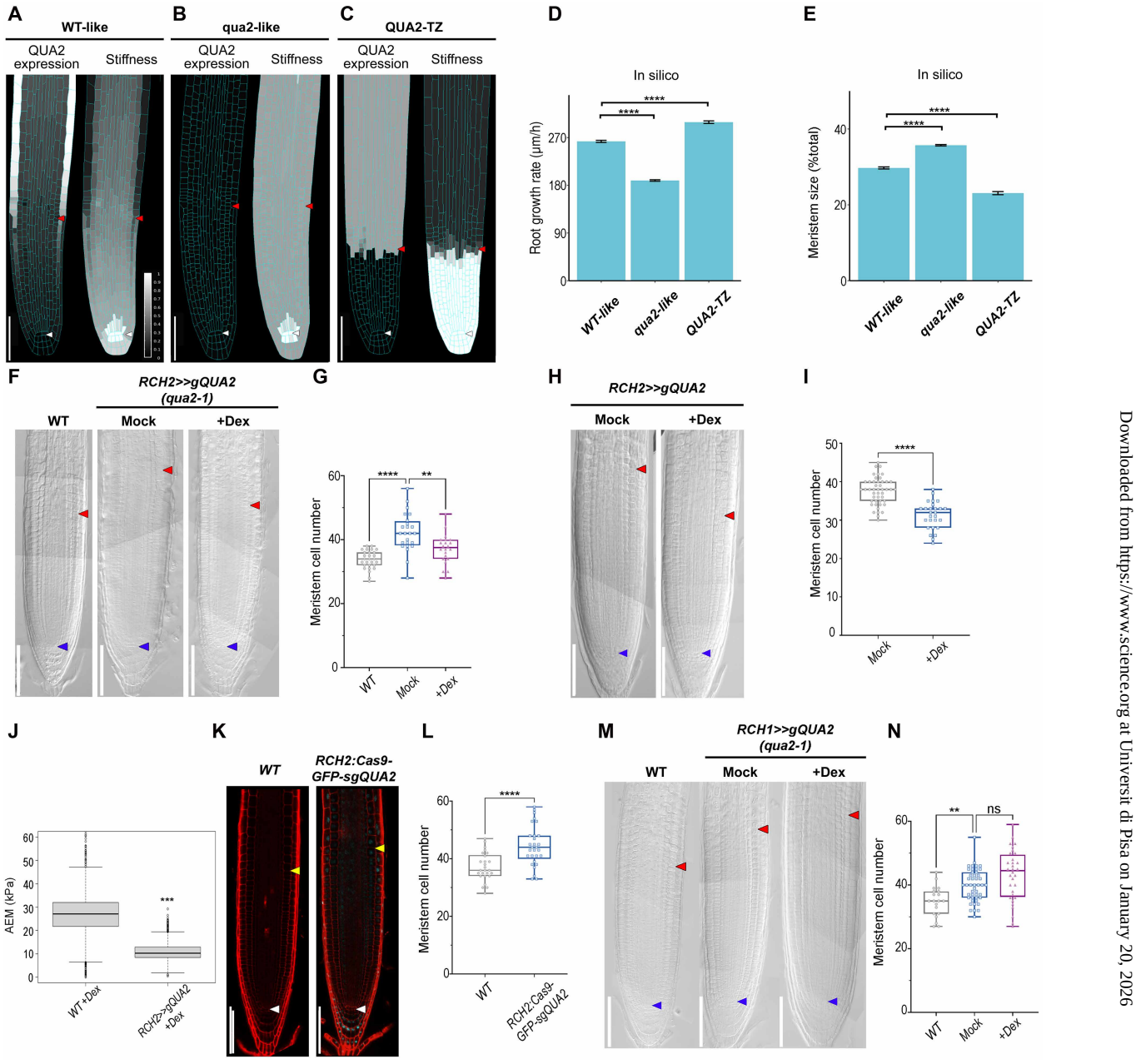

Fig. 3. Elongating cell wall loosening limits cell division of meristematic cells. (**A** to **C**) Computational simulations of roots with different QUA2 expression patterns: WT (A), no expression (qua2-like, B), and restricted to the TZ (C). First: *QUA2* expression; second: stiffness distribution. Color bars indicate relative intensities. Red and white arrowheads mark the TZ and QC, respectively. (**E**) Quantification of root growth rate (micrometers per hour) and meristem size (percentage of total length) from in silico simulations. Data represent means ± SE. ****$P \leq 0.0001$, Welch's *t* test. (**F**) Differential interference contrast (DIC) microscopy of WT, *RCH2>>gQUA2* (*qua2-1*), and *RCH2>>gQUA2* (*qua2-1*) upon Dex induction. Red arrowheads mark the TZ, and blue arrowheads mark the QC. (**G**) Meristem cell number relative to (F). **$P \leq 0.01$ and ****$P \leq 0.0001$, one-way analysis of variance (ANOVA) with Tukey's post hoc test. $n = 28$, 24, and 22, $N = 3$. (**H**) DIC microscopy of *RCH2>>gQUA2* roots in mock and Dex conditions. Red arrowheads mark the TZ, and blue arrowheads mark the QC. (**I**) Meristem cell number relative to (H). ****$P \leq 0.0001$, unpaired Student's *t* test. $n = 46$ and 27, $N = 3$. (**J**) Box plot of AEM from WT (four seedlings, 2605 curves) and *RCH2>>gQUA2* (five seedlings, 2753 curves). WT modulus (26.84 ± 7.88 kPa) was significantly higher than *RCH2>>gQUA2* (10.65 ± 3.40 kPa), 152% increase, ***$P \leq 0.001$, Mann-Whitney *U* test. (**K**) Confocal images of WT and *RCH2:Cas9-GFP-sgQUA2* roots. Yellow arrowheads mark the TZ, and white arrowheads mark the QC. (**L**) Meristem cell number relative to (K). ****$P \leq 0.0001$, unpaired Student's *t* test. $n = 26$ and 29, $N = 3$. (**M**) DIC microscopy of WT, *RCH1>>gQUA2* (*qua2-1*), mock and Dex roots. Red arrowheads mark the TZ, and blue arrowheads mark the QC. (**N**) Meristem cell number relative to (M). **$P \leq 0.01$ and not significant (ns), Brown-Forsythe and Welch ANOVA with Dunnett's test. $n = 20$, 46, and 32, $N = 3$. Scale bars, 100 µm.

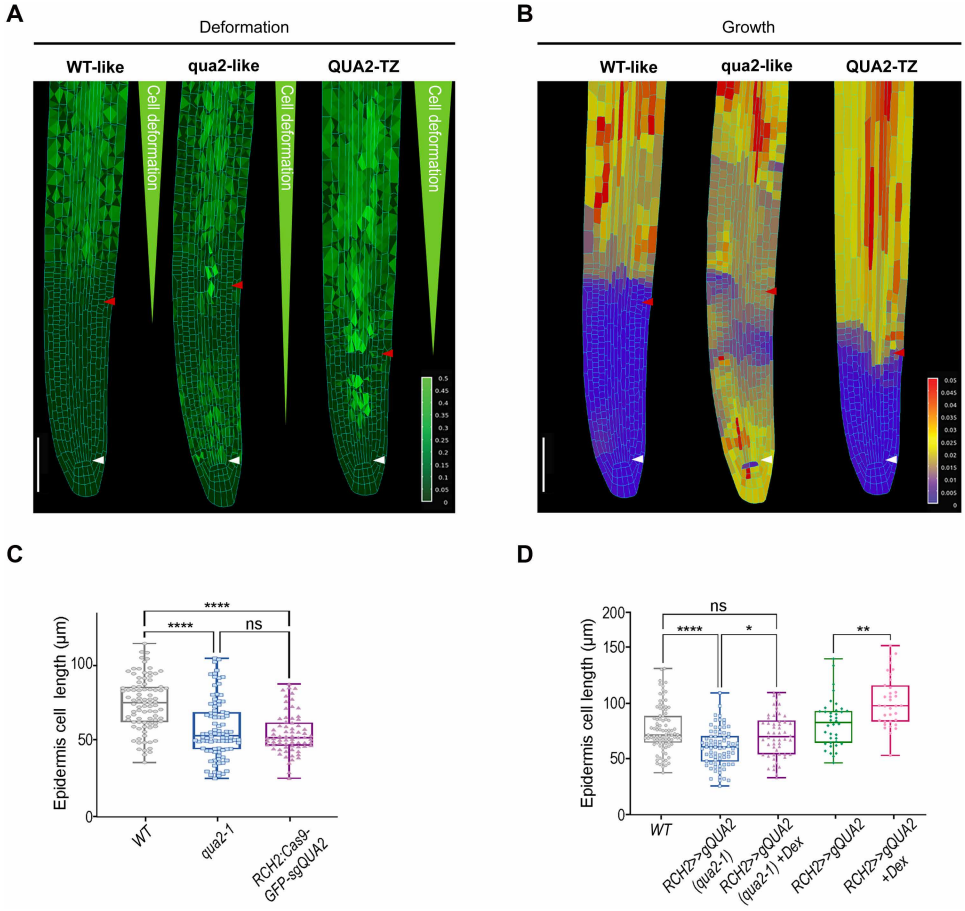

Fig. 4. Changes in meristem size correlate with dynamic cell deformation and root growth. (**A** and **B**) Computational model simulations reporting WT-like, qua2-like, and QUA2-TZ cell deformation (A) and cell growth (B). Red arrowheads and white arrowheads indicate the TZ and the QC, respectively. (**C**) Length of in vivo elongating epidermal cells of WT, qua2-1, and RCH2:Cas9-GFP-sgQUA2. ****$P \leq 0.0001$ and not significant (ns), Kruskal-Walis with Dunn's post hoc test for multiple comparisons. $n = 90$, 92, and 70, $N = 3$. (**D**) Length of in vivo elongating cortical cells of WT, qua2-1; RCH2>>gQUA2 (qua2-1) mock and upon Dex (+Dex), and RCH2>>gQUA2 mock and upon Dex (+Dex). ****$P \leq 0.0001$, ***$P \leq 0.001$, *$P \leq 0.05$, and not significant (ns). Ordinary one-way ANOVA with Tukey's post hoc test multiple comparisons and Mann-Whitney *U* test. $n = 93$, 79, 55, 39, and 35, $N = 3$.

The *qua2-1* mutant and the pRCH2:Cas9-GFP-sgQUA2 plants exhibited shorter differentiated cells than WT plants (Fig. 4C and fig. S4B). In contrast, *RCH2>>gQUA2* (*qua2-1*) plants exhibit an increase in the size of differentiated cells, reaching dimensions comparable to those of WT, while in *RCH2>>gQUA2* plants, cells were even longer than WT (Fig. 4D and fig. S4C). In plants where QUA2 expression did not change the size of the meristem, such as *RCH1>>gQUA2* (*qua2-1*), the size of differentiated cell was unaffected (fig. S4D). Thus, in agreement with model simulations, plants with a longer meristem displayed shorter differentiated cells, whereas plants with a shorter meristem exhibited longer differentiated cells.

To test whether changes in the cell size of differentiated cell was accompanied to changes in the cell elongation rate, we performed live imaging confocal experiments to examine cell growth dynamic in WT, *qua2-1* mutant, and *RCH2>>gQUA2* roots (Fig. 5, A to F, and movies S3 and S4). Specifically, we measured the average cell area over time in the EZ (Fig. 5, A, B, D, and E) and calculated expansion rates (square micrometers per minute) via linear regression (Fig. 5, C and F). These analyses confirmed that in the *qua2-1* mutant, the growth rate of elongating cells is reduced while, in *RCH2>>gQUA2* roots, was enhanced as predicted by model simulations.

According to our model, changes in cell size and elongation rate generate mechanical constraints that interfere with the division capacity of meristematic cells, ultimately leading to the observed changes in meristem size. To verify whether changes in cell size and elongation rate precede and drive subsequent alterations in meristem size, we performed a time-course complementation analysis of the *qua2-1* mutant, achieved by expressing QUA2 protein under its native promoter [*QUA2-GVG-ter-6xUAS-mCITRINE-gQUA2* (*QUA2>>gQUA2*)] in the mutant background [*QUA2>>gQUA2* (*qua2-1*)]. Cells reach full complementation at 16 hours, whereas detectable changes in meristem size occur only at 24 hours, corroborating the idea that alterations in the meristem follow cell elongation dynamics at the TZ (Fig. 5, G and H).

A plausible explanation for how elongating cells influences the division capacity of meristematic cells is that their expansion generates mechanical constraints affecting the growth of neighboring dividing cells, thereby modulating rate mitotic activity and meristem growth. To analyze cell growth dynamics of dividing cells, we performed live

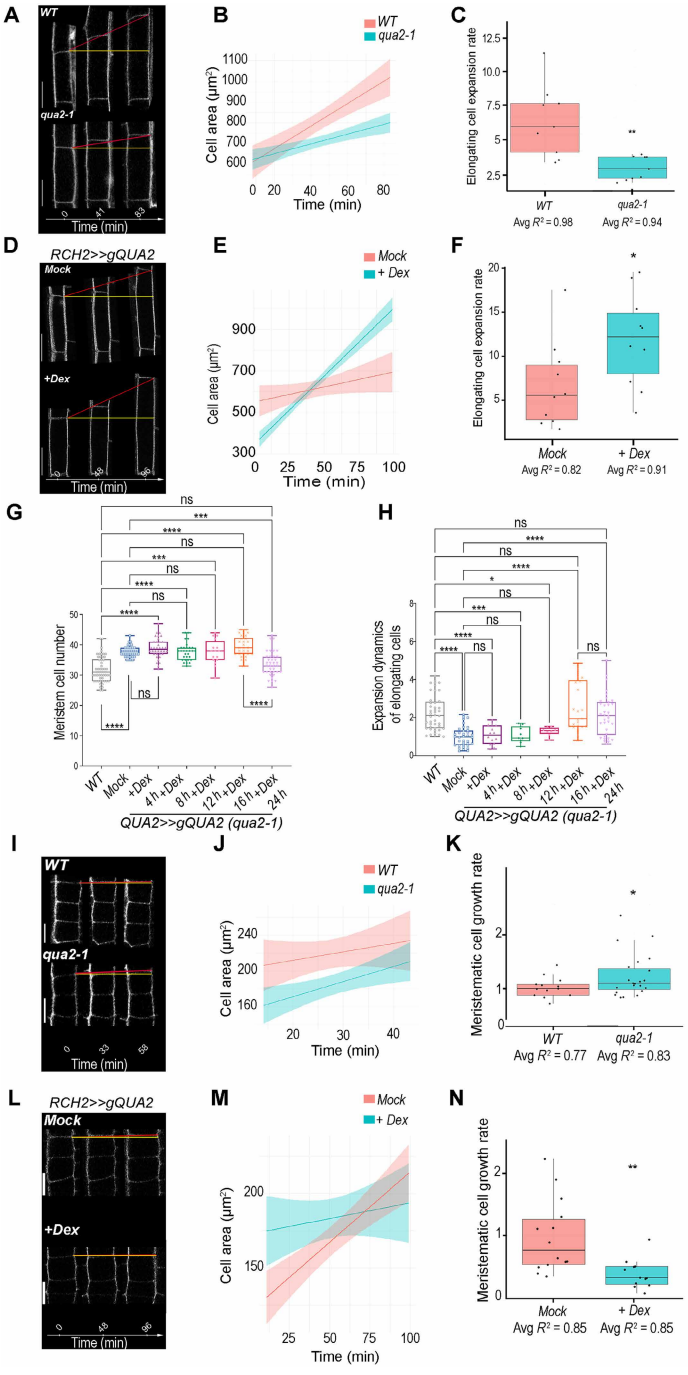

Fig. 5. Mechanical constraints generated by elongating cells control cell division in the meristem. (**A** and **D**) Representative stacks of elongating epidermal cells in the EZ of WT, *qua2-1*, and *RCH2>>gQUA2* mock versus Dex, showing reduced expansion of *qua2-1* versus WT and enhanced elongation in *RCH2>>gQUA2* upon Dex induction relative to mock. Yellow lines indicate the initial cell size ($t = 0$), and red lines indicate the final size after 83 and 96 min. Scale bars, 25 µm. (**B** and **E**) Linear regression of elongating cell area (square micrometers) over time (minutes) in WT, *qua2*-1, and *RCH2>>gQUA2* mock versus Dex, with 95% confidence intervals. (**C**) Cell expansion rate of WT versus *qua2-1* elongating cells. $^{**}P \leq 0.01$, Mann-Whitney *U* test. $n = 9$ and 9. (**F**) Expansion rate of RCH2>>gQUA2 cells mock versus Dex. $^{*}P \leq 0.05$, unpaired *t* test. $n = 10$ and 10, $N = 3$. (**G**) Root meristem cell number of WT and *QUA2>>gQUA2* (*qua2-1*) mock versus Dex induction at 4, 8, 12, 16, and 24 hours (h). $^{****}P \leq 0.0001$, $^{***}P \leq 0.001$, and not significant (ns), Kruskal-Wallis with Dunn's post hoc test. $n = 54, 41, 36, 30, 16, 30$, and 37, $N = 3$. (**H**) Expansion dynamics of elongating cells, same as (G). $^{****}P \leq 0.0001$, $^{***}P \leq 0.001$, $^{*}P \leq 0.05$, and not significant (ns), Kruskal-Wallis with Dunn's post hoc test. $n = 44, 36, 14, 9, 25, 25$, and 34. (**I** and **L**) Representative stacks of meristematic epidermal cells in the DZ of WT, *qua2-1*, and *RCH2>>gQUA2* mock versus Dex treatment, showing increased growth rate in *qua2-1* and reduced rate in *RCH2>>gQUA2* Dex-treated roots. Yellow lines mark the initial cell size ($t = 0$), and red lines mark the final size after 58 and 96 min. Scale bars, 25 µm. (**J** and **M**) Linear regression of cell area (square micrometers) over time in WT, *qua2-1*, and *RCH2>>gQUA2* mock versus Dex, with 95% confidence intervals. (**K**) Growth rate of WT versus *qua2-1* meristematic cells. $^{*}P \leq 0.05$, Welch's *t* test. $n = 12$ and 22, $N = 3$. (**N**) Growth rate of *RCH2>>gQUA2* mock versus Dex. $^{**}P \leq 0.01$, Mann-Whitney *U* test. $n = 15$ and 12, $N = 3$.

imaging experiments in WT, *qua2-1*, and *RCH2>>gQUA2* root meristems (Fig. 5, I to K, and movies S5 and S6). These analyses revealed that the *qua2-1* mutant growth rate and the average growth area of meristematic cells are increased compared to WT plants (Fig. 5, J and M), while those of the *RCH2>>gQUA2* roots decrease in agreement with computer model simulations (Fig. 5, L to N).

These data corroborate model predictions where mechanical constraints generated by the expansion of elongating cells act on meristematic cell growth thus fine-tuning their division activity, controlling root and root meristem growth (Fig. 6). Nevertheless, it should be pointed out that, although the effects of these constraints are evident, they should be regarded as a plausible hypothesis until future technological advances allow direct measurements.

DISCUSSION

Mechanical forces have long been recognized as key players in shaping multicellular biological systems (*28*–*33*). The strength and direction of these forces interact with cellular and tissue properties such as elasticity and stiffness, which determine how tissues respond to mechanical loads and, in turn, influence cell shape, size, and activity. In animal systems, the extracellular matrix (ECM) plays a central role in determining mechanical properties, with biochemical alterations in the ECM profoundly affecting organogenesis, stem cell behavior, cell fate, and even tumor progression (*34*–*37*).

While mechanical signaling is also critical in plants, much less is known about how these cues are integrated into organ development. In plants, cells are encased in a rigid cell wall, meaning that their growth is physically constrained also by their neighbors. As a result, the mechanical properties of the cell wall not only shape individual cells but also influence adjacent ones, potentially directing their behavior.

To uncover these dynamics, we combined genetics, live imaging, two independent approaches—noninvasive Brillouin microscopy imaging and AFM for mechanical measurements, and advanced computational modeling. Our findings suggest that mechanical constraints exerted by elongating root cells act as a physical brake on adjacent dividing cells, limiting their proliferation and defining both meristem size and the TZ position during root development. This mechanical influence is directly tied to the elastic properties of cell walls in the EZ. In the *qua2-1* mutant, increased cell wall stiffness in the EZ restricts expansion, releasing the mechanical restraint on meristematic cell division. Conversely, QUA2 overexpression at the TZ softens cell walls, enhancing the mechanical brake and further restricting cell proliferation in the meristem, resulting in meristem shortening.

Mechanical constraints from neighboring elongating cells can influence the size of meristematic cells by altering the time they need to reach the critical size for division. This, in turn, affects the frequency of cell division, leading to expansion or shrinkage of the meristem. A similar mechanism has been described in yeast, where cells sense their own size and regulate division timing through dilution of transcription factors (*38*–*41*). In *Arabidopsis*, it is plausible that changes in cell size could similarly affect the intracellular concentration of key morphogenetic regulators, such as auxin or PLETHORA transcription factors (*7*, *40*–*42*). When a cell is mechanically constrained and

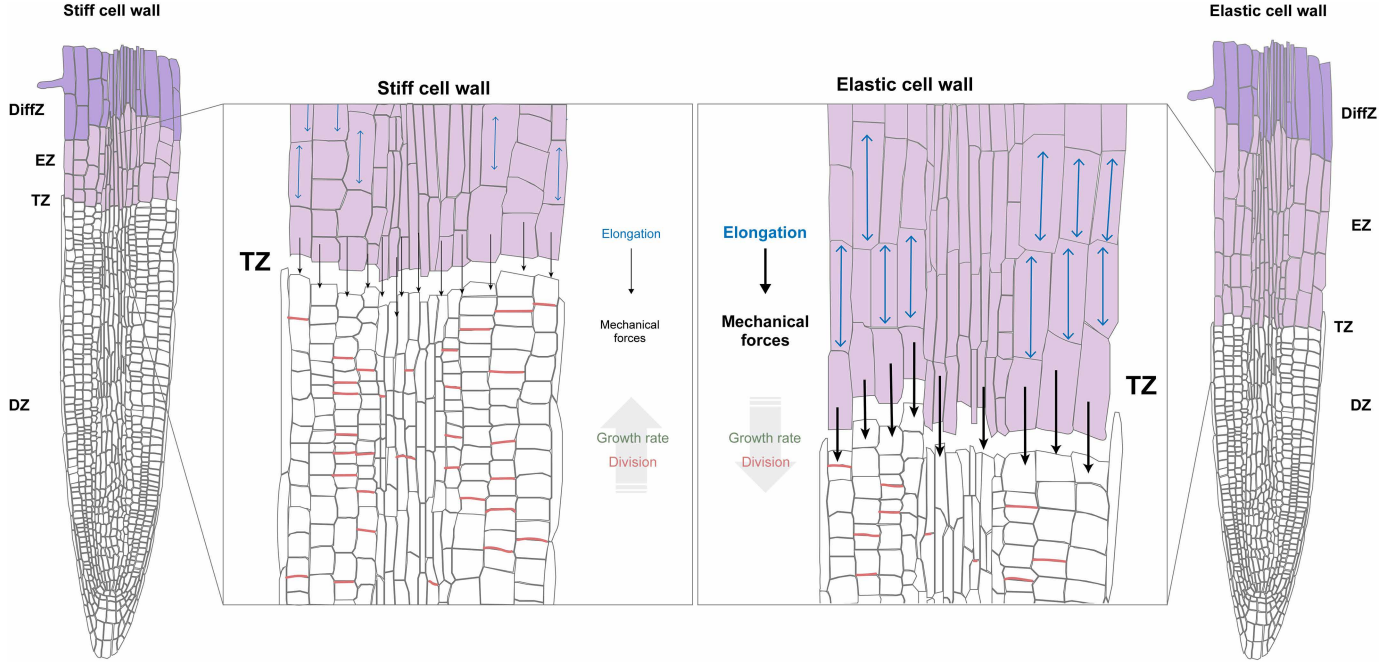

Fig. 6. Mechanical constraints from the EZ regulate meristem size. Elongating cells in the root exert mechanical constraints on adjacent meristematic cells, acting as a physical brake that limits their proliferation. This regulation is mediated by the elastic properties of the cell walls in the EZ. Meristematic cells respond to changes in the intensity of mechanical constraint by adjusting the time required to reach the critical size for division, thereby modulating their division frequency and ultimately determining meristem size. In the *qua2-1* mutant (left), increased cell wall stiffness in the EZ restricts cell expansion, weakening the mechanical constraint on the meristem. This release of tension promotes the growth and division of meristematic cells, leading to an expanded meristem. Conversely, QUA2 overexpression at the TZ (right) softens the cell walls, enhancing the mechanical constraint on the meristem. This increased tension reduces cell growth and proliferation, resulting in a shortened meristem.

its volume is reduced, these factors could become more concentrated, potentially enhancing their activity. Conversely, if the cell expands, the concentration of these factors could decrease, modulating their signaling output. Thus, mechanical constraints could indirectly shape cellular behavior by modulating the internal gradients of key regulatory molecules, linking physical cues to biochemical responses.

In conclusion, we propose the cell wall and its mechanical properties as an important source of both cell-autonomous (i.e., local changes in wall composition) and cell-nonautonomous (i.e., mechanical constraints on neighboring cells) signals that can profoundly influence the behavior of cells and thus the development of entire organs.

A key future challenge will be to decipher how mechanical signals integrate into molecular networks to locally control cell activity and determine whether specific mechanosensor(s) translate these physical forces into biological responses. Unraveling these mechanisms will open frontiers in our understanding of organ development and growth regulation.

MATERIALS AND METHODS

Plant material and growth conditions

All mutants are in the *A. thaliana* ecotype Columbia-0 (Col-0). *ixr1-2*, *mur4-2*, *gaut10-2*, and *gaut10-3* were obtained from the Nottingham Arabidopsis Stock Centre (NASC) collection (NASC IDs: N6202, N8569, N675953, and N592577, respectively). *qua2-1* was previously described in (*19*). The *qua2-1* mutant was genotyped by Derived Cleaved Amplified Polymorphic Sequences (dCAPS) (*43*) and/or sequencing. For dCAPS, the PCR product has been amplified by using *qua2-1*-dCAPS_Fw and *qua2-1*- dCAPS_Rev (see table S6). The amplicon was digested with SpeI for 16 hours at 37°C. The PCR product for sequencing was amplified with the following oligos: *qua2-1*-seq_Fw and *qua2-1*-seq_Rev (see table S6). The *qua2-5* mutant was generated via CRISPR-Cas9 technology (see the "CRISPR-Cas9 mutagenesis" section). The mutation was genotyped via sequencing with the following oligos: *qua2-5*_Fw and *qua2-5*_Rev (see table S6). *CYCB1;1:GUS* and *RCH1-GFP* have been described previously in (*4*). *CYCB1;2:GFP* was previously described in (*21*). For growth conditions, *A. thaliana* seeds were surface-sterilized, and seedlings were grown on one-half strength Murashige and Skoog (MS) medium containing 0.8% agar at 22°C in long-day conditions (16-hour light/8-hour dark cycle) as previously described in (*44*).

Root length, meristem size, and cell length analysis

For root length measurements, plates were photographed, and the resulting images were analyzed using the image analysis software ImageJ 1.54g available online (http://rsbweb.nih.gov/ij/). Root meristem size is expressed as the number of meristematic cortex cells in a file, extending from the quiescent center (QC) to the first longitudinally elongated cortex cell, as described in (*44*). The cortex is the most suitable tissue for counting meristematic cells, as it consists of a single cell type and maintains a conserved number of cells across different *Arabidopsis* roots. The analyses were performed starting from 5 days postgermination, when the meristematic cell number is settled. To assess the elongation capacity of epidermal and cortical root cells, cell length of the first epidermal cells exhibiting the initial hair bulge or on the nearest cortical cell was measured using ImageJ. To assess cell expansion dynamics of epidermal root cells, cell length of the first five epidermal cells was measured using ImageJ. Cell expansion dynamics were quantified by calculating cell deformation as the slope of a linear regression of cell length plotted against cell rank relative to the TZ. The TZ was assigned rank 0; the first elongating cell analyzed was assigned rank 1, up to rank 5 for the most distal cell included in the analysis.

DIC and confocal microscopy

Differential interference contrast (DIC) with Nomarski technology microscopy (Zeiss Axio Imager A2 or an Axioskop 2 plus) was used to count the meristem cell number with a dry 40× objective. Plants were mounted in a chloral hydrate solution (8:3:1 mixture of chloral hydrate:water:glycerol) and immediately analyzed at the microscope (*44*). For confocal microscopy, cell walls from 6 days postgermination were stained with 30 μM propidium iodide (PI) solution (30 μg/ml). Images were acquired using Zeiss LSM 780 or a Zeiss LSM 900 confocal microscope with an oil immersion 40× objective. Laser lines and imaging settings were selected according to the staining dyes and fluorescent proteins used in the analysis. Images were analyzed with ImageJ and eventually stitched and postprocessed with Adobe Photoshop CS2. Image postprocessing was minimal and restricted to corrections in brightness and contrast. All corrections were uniformly applied to the entire images so that all final figures properly reflect the original data.

B-glucuronidase (GUS) histochemical assay

To visualize *CYCB1;1:GUS* lines, GUS histochemical assay was performed using the β-glucuronidase substrate X-gluc (5-bromo-4-chloro-3-indolyl glucuronide, Duchefa) dissolved in *N-N*-dimethylformamide. X-gluc solution, composed of 100 mM Na_2HPO_4, 100 mM NaH_2PO_4, 0.5 mM $K_3Fe(CN)_6$, 0.5 mM $K_4Fe(CN)_6$, 0.1% Triton X-100, and X-gluc (1 mg/ml), was prepared as previously described. Seedlings were incubated at 37°C in the dark for 4 hours.

Drug and hormone treatments

For induction assays, 5 days postgermination *RCH2-GVG-mCITRINE-gQUA2* (*qua2-1*), *RCH2-GVG-mCITRINE-gQUA2* (Col-0), *RCH1-GVG-mCITRINE-gQUA2* (*qua2-1*), and *RCH1-GVG-mCITRINE-gQUA2* (Col-0) seedlings were transferred with tweezers onto solid ½ MS medium supplemented with 10 μM Dex water-soluble (Sigma-Aldrich) and incubated overnight. For the time-course complementation analysis, *pQUA2-GVG-mCITRINE-gQUA2* (*qua2-1*) and *pQUA2-GVG-mCITRINE-gQUA2* (Col-0) seedlings were transferred onto ½ MS medium containing 10 μM Dex and incubated for 4, 8, 12, 16, or 24 hours. For trans-zeatin treatment, 5 days postgermination WT and *qua2-1* seedlings were transferred onto solid ½ MS medium supplemented with 5 μM trans-zeatin and incubated overnight.

Live imaging analyses

Root images were obtained using a live imaging approach via confocal microscopy. For live imaging analyses, 6 days postgermination plants were mounted in Ibidi μ-Dish 35-mm chambers. *RCH2>>gQUA2* roots were induced for one overnight before starting the analysis. The roots were positioned at the center of the observation area with a drop of water and then covered with a thin layer of solidified MS medium supplemented with PI (50 μg/ml) to allow root staining. Images were acquired using a Zeiss LSM 780 confocal microscope with an oil immersion 40× objective. To assess the growth rate of meristematic cells and the expansion rate of elongating cells, we measured the epidermal cell area in cells from equivalent root zones and developmental stages of different roots. Measurements were performed on selected cells for each time point by using ImageJ. The cell surface measurements were plotted on average and as a function of time (minutes), and confidence

intervals were represented on each graph to highlight data distribution. Growth rates were computed as the slope of the linearly regressed cell surface growth overtime for each cell. Cells growing nonlinearly ($R^2 < 0.70$) were neglected.

CRISPR-Cas9 mutagenesis

To obtain *qua2-5* allele, a single guide RNA (sgRNA) of 20 nucleotides was designed using CRISPR/Cas9 target online predictor (CCTOP) (*45*, *46*) to target the first exon of *QUA2*. Oligos corresponding to the target sequence (sgQUA2_Fw and sgQUA2_Rev; see table S6) were annealed by heating at 95°C for 10 min and then slowly cooled to room temperature. The annealed oligos were subsequently ligated into the TSKO destination vector, specifically the F-G entry vector, following the standard cloning procedures. The vector was first digested with AarI according to the manufacturer's recommendations to generate four base pair overhangs suitable for direct guide RNA (gRNA) loading. The digestion reaction (20 µl) included 1 µg of plasmid DNA, 0.5 µM oligonucleotides, 1 U of AarI, and 1× buffer in Milli-Q water. The mix was incubated at 37°C for 4 hours, followed by enzyme inactivation at 65°C for 20 min. To generate the construct, the *RPS5A* promoter was used to guide the Cas9 and the sgRNA. For the generation of the RPS5A:Cas9-GFP-sgQUA2 construct, a Golden Gate reaction was carried out using the components listed in table S1 and the conditions reported in table S2.

Primary transformants were selected using phosphinothricin (PPT) resistance. Ten independent T_2 lines were initially screened for phenotypic traits. Genomic DNA was then extracted using the Geneaid DNA extraction kit and analyzed via Sanger sequencing with the oligos *qua2-5*_Fw and *qua2-5*_Rev (see table S6). To determine the mutation, sequencing results were first analyzed using Tracking of Indels by DEcomposition (TIDE) (http://shinyapps.datacurators.nl/tide/) and subsequently aligned with the WT sequence using MultAlin (http://multalin.toulouse.inra.fr/multalin/). The predicted protein sequence was further examined using Expasy Translate (https://web.expasy.org/translate/).

Generation and characterization of transgenic plants

Standard molecular biology techniques, the Gateway system (Invitrogen), and the Green Gate System were used for the cloning procedures. For *pRCH2-3xYFP* construct, the *p4p1-pRCH2* vector was provided by R. Heidstra (Wageningen University, the Netherlands); the LR (Thermo Fisher Scientific) reaction was performed by using *p4p1-pRCH2*, the *pDONOR221-3xYFP*, a C-term *pDONORP2P3-NOST2*, and *pBm43GW*. The reaction was performed as indicated in table S3.

The mix was incubated at room temperature for 16 hours, followed by enzyme inactivation with proteinase K at 37°C for 10 min. For the *pQUA2-mGFP-gQUA2* construct, the promoter sequence of QUA2 (AT1G78240) [3562 base pair (bp)] was amplified by using the pQUA2_Fw and pQUA2_Rev oligos (see table S6), and the PCR product was then cloned into *pDONORP4P1* vector via BP reaction. The reaction was performed as reported in table S4. The mix was incubated at room temperature for 16 hours, followed by enzyme inactivation with proteinase K at 37°C for 10 min.

The genomic sequence of QUA2 (2640 bp) was amplified using the gQUA2_Fw and gQUA2_Rev (see table S6) and cloned in pDONORP2P3 via BP reaction (see above). The sequence of mGFP (717 bp) was amplified from pGG-C-Cas9PTA-D (*27*) by using the mGFP_Fw and mGFP_Rev oligos (table S7) and cloned in pDONORP221 via BP reaction (see above). For the generation of the pQUA2-mGFP-gQUA2 construct, a LR reaction was performed by using pDONORP4P1-pQUA2, pDONOR221-mGFP, and pDONORP2P3-gQUA2. pQUA2-GVG-ter-6xUAS-mCITRINE-gQUA2, pRCH1-GVG-ter-6xUAS-mCITRINE-gQUA2, and pRCH2-GVG-ter-6xUAS-mCITRINE-gQUA2 were generated via a LR reaction between pDONORP4P1-pQUA2 or pDONORP4P1-RCH1 or pDONORP4P1-RCH2, respectively, pDONOR221-GVG-ter-6xUAS-mCITRINE [CS2106294, NASC ID: N2106294; (*47*)] and pDONORP2P3-gQUA2. The LR products were then subcloned in the Gateway pBm43GW destination vector (see above). All constructs were sequenced before transformation via floral dipping, and homozygous plants were isolated by using PPT (Duchefa) as the selective marker. pQUA2-mGFP-gQUA2 fusion was tested to be functional by rescuing *qua2-1* mutant phenotype.

Tissue-specific knockout (CRISPR-TSKO) RCH2:Cas9-GFP-sgQUA2 construct was obtained as reported in (*27*). The sequence of RCH2 promoter (2313 bp) was amplified by using the pRCH2_Fw and pRCH2_Rev oligos (see table S6) and cloned in the A-B entry module (pGG-A-LinkerIII-B). The same sgRNA previously used for CRISPR-Cas9 mutagenesis (see the "CRISPR-Cas9 mutagenesis" section) was used for this construct. To generate the gRNA, complementary oligonucleotides were annealed by heating at 95°C for 10 min and then slowly cooled to room temperature. The annealed oligos were subsequently ligated into the TSKO destination vector, specifically the F-G entry vector, following the standard cloning procedures. The vector was first digested with AarI according to the manufacturer's recommendations to generate four base pair overhangs suitable for direct gRNA loading. The digestion reaction (20 µl) included 1 µg of plasmid DNA, 0.5 µM oligonucleotides, 1 U of AarI, and 1× buffer in MQ water. The mix was incubated at 37°C for 1 to 16 hours, followed by enzyme inactivation at 65°C for 20 min. The generation of the RCH2:Cas9-GFP-sgQUA2, a Golden Gate reaction, has been performed by incorporating the components described in table S5. The reaction was performed as reported in table S2.

Cell division rate measurements

The cell division rate was calculated as previously described (*4*). Walls of 6-day-old seedlings were stained with 30 µM PI solution (30 µg/ml). Z-stack images of entire roots were acquired using a Zeiss LSM 780 or Zeiss LSM 900 confocal microscope with a 40× oil immersion objective. Laser settings were adjusted according to the excitation/emission properties of PI and the fluorescent protein under analysis. Images were processed and analyzed using ImageJ. The root meristem cell number was quantified as the number of cortex cells in a single cortical cell file, spanning from the QC to the first elongated cell. The cell division rate (X/Y) was calculated as the ratio between the number of GFP-expressing cells (X) and the total meristem cell number for each root (Y).

Fluorescence quantification

Quantification of *pQUA2-mGFP-gQUA2* was obtained as reported in (*44*). The mean gray value of the GFP channel of confocal laser scanning microscope images was measured with the software ImageJ (https://imagej.nih.gov/ij/). Fluorescence intensity was normalized to the corresponding tissue area to ensure accurate quantification. For longitudinal quantification, a segmented line was drawn along

the longitudinal axis of the epidermis, the tissue exhibiting the highest QUA2 expression. Fluorescence intensity profiles were extracted, and the mean gray value was calculated as a function of the distance from the QC, defined as position zero. Individual fluorescence profiles from a statistically significant number of roots were averaged to obtain the mean longitudinal intensity distribution. The averaged curves were smoothed and denoised in GraphPad Prism using a second-order polynomial and averaging 50 neighboring values. Nonlinear regression was then performed using the Gaussian function $Y = Y_0 + A * \exp[-(X - X_c)^2/(2 * \sigma^2)]$, where Y_0 represents the baseline fluorescence, $A = Y_{max} - Y_0$, σ was fixed at full width at half maximum divided by 2.355 (estimated at 300), and X_c corresponds to the position of Y_{max}. The fit resulted in an R^2 of 0.96, allowing reliable identification of the peak fluorescence position. Confidence intervals (95%) were calculated, and the maximum fluorescence peak was indicated in the plots by a red line.

RNA isolation and RT-qPCR

Total RNA was extracted from root tissues using the NucleoSpin RNA Plus (Macherey-Nagel). The quality of isolated RNA was checked using a NanoDrop 1000 spectrophotometer (Thermo Fisher Scientific).

For RT-qPCR, the cDNA was retrotranscribed using the SuperScript III First-Strand VILO cDNA Synthesis Kit (Thermo Fisher Scientific). RT-qPCR analysis was performed using the gene-specific oligos (see table S6) previously described in (*5*, *48*). Amplification was monitored in real time with a 7500 Real Time PCR System (Applied Biosystems). ACTIN2 (AT3G18780) was used as a housekeeper control. Shown data are expressed in $2^{-\Delta\Delta Ct}$. Three technical replicates of RT-qPCR were performed on three independent RNA batches. Results were comparable in all the experiments and with the housekeeper.

Statistical analysis

Statistical analysis was performed using GraphPad software (http://graphpad.com). For all experiments, analyses were performed in three biological replicates, while the number of analyzed sample is reported in figure legend. No statistical sample size predetermination nor randomization was undertaken. The investigators were not blinded to allocation during experiments and outcome assessment. Data exclusion was performed via a Graph test [robust linear model regression and outlier removal (ROUT) method, $Q = 10\%$]. Identified outliers were removed from the statistical analyses. All the statistical details of each experiment (including—whenever present—the statistical tests used, values of *n*, mean, SD, SE, and confidence intervals) can be found in the corresponding figure legend. For all figures, representative pictures of samples were chosen. In figures, statistical significance is conventionally indicated by *, and the *P* value is reported in the corresponding figure legend.

AFM nanoindentation experiments

We used an atomic force microscope (BioScope Catalyst, Bruker, Billerica, MA, USA) coupled to an optical inverted microscope (Olympus IX81, Miami, FL, USA) to conduct indentation analysis. Seedlings were attached to petri dishes with a thin layer of silicone glue (Pegamil, Anaerobicos SRL, Buenos Aires, Argentina). Roots from 7-day-old seedlings were studied using an AFM fluid cantilever holder at 25°C. All AFM measurements were performed within 1 hour after insertion of the AFM head. The silicon nitride probe (DNP-10, cantilever A; Bruker, Billerica, MA, USA), with a tip radius of 20 nm, was attached to a triangular 175-μm-long cantilever with a spring constant of 0.35 N/m, following the manufacturer's instructions. For indentation, we positioned the cantilever using a ×20 magnification eyepiece on the surface of the epidermal cells of the TZ of the primary root using the Contact Fluid - Point & Shoot, positioning it in the center of the cell. We set a low (1 Hz) frequency to maximize the number of captured force curves, as previously described (*49*, *50*). We obtained force curves in 30 points distributed in an area of 500 nm^2. We captured at least 300 force curves for each cell. We obtained the apparent Young's modulus (AEM) from first- and second-order polynomial fits of the obtained force curves, according to (*51*), considering an indentation depth of 100 nm of each curve to avoid the effect of the substrate on the stiffness measurements. We discarded force curves with a correlation coefficient lower than 0.99. A normalized histogram of the remaining data was created and fitted with a Gaussian distribution. We then discarded data points outside the 95% confidence interval and recalculated the histogram and the Gaussian fit. A Student's *t* test was used to determine statistical significance between groups. We analyzed three genotypes, and a $P < 0.05$ was considered significant.

Brillouin microscopy measurements

Our custom-built confocal Brillouin microscope is described elsewhere (*52*). Briefly, it consists of an inverted microscope (Olympus IX-73) coupled to a double virtually imaged phased array–based spectrometer (*24*) through single-mode optical fibers. The three-dimensional mechanical properties of samples are recovered in a label-free, contactless manner through confocal laser scanning mode thanks to a pair of galvanometric mirrors (Thorlabs) and a piezo stage (MadCity Labs). The laser source is a continuous-wave single-mode laser at a 532-nm wavelength (Oxxius).

High-resolution Brillouin maps of cell walls were obtained via a 60× objective [Olympus, numerical aperture (NA) = 1.40] in backscattering configuration with a spatial resolution of a confocal microscope. During Brillouin data acquisitions of the cell wall, the stage longitudinal step size on the sample was 200 nm, the acquisition time was 100 ms per point, and the optical power delivered to the specimen was 15 mW, ensuring no optical damage to the sample.

Aside from the Brillouin laser-scanning module, a standard brightfield and fluorescence spinning-disk unit (Crest Optics X-LIGHT V1) is in the side port of the microscope to retrieve morphological and fluorescent information of the sample on the same plane and at the same time as Brillouin microscopy. The setup is controlled in MATLAB via a custom-built graphical user interface.

Pixel-to-gigahertz conversion was obtained from the signals of an electro-optic phase modulator (*23*). Brillouin curves were fitted with sum of Lorentzian distributions, from which we extrapolated the Brillouin shift values: Higher Brillouin shifts have been proved to be reliable indicators of stiffness (*23*, *24*, *53*, *54*) especially in *A. thaliana* samples (*55*, *56*).

Fresh seedlings were stained with calcofluor white (1 g/liter, Sigma-Aldrich) for 1 hour at room temperature. After staining, they were mounted on a 1-mm coverslip with a few drops of distilled water. A 0.17-mm coverslip was then placed on top, and the edges were sealed with nail polish to prevent evaporation. In such a manner, the buffer never evaporated, and the tissues were kept hydrated during acquisitions; its presence was confirmed by its Brillouin shift, similar to water. We localized the TZ of the seed in brightfield via a large field

of view objective (i.e., a 10×); then, we switched to a high magnification, small field of view (60×, NA = 1.4) objective, used for bright-field, confocal fluorescence, and Brillouin acquisitions. We used data obtained from calcofluor white fluorescent signals as masks and averaged Brillouin shifts over them; data shown in Fig. 2B are mean Brillouin shifts calculated over these masks. No manipulations have been applied to Brillouin maps for visualization of data. All data analysis has been performed using custom-made MATLAB codes.

Spatio-temporal root growth model simulations

Mechanical growth model framework

The model was implemented within the MorphoDynamX/MorphoGraphX modeling toolset, a powerful environment designed for studying plant growth and form in biological systems (*57*). The core data structure in MorphoDynamX is organized around the concept of cell complexes, a versatile framework for representing cellular and subcellular geometries in computational biology (*58*).

The biomechanics module leverages a position-based dynamics (PBD) framework, a robust and efficient approach to simulating mechanical behavior (*59*). This PBD framework has been further refined and developed in our laboratory (*26*). Growth is driven by uniform internal turgor pressure, whereas mechanics is modeled using a constraint-based implicit method, which is particularly effective for simulating physical phenomena such as viscoelastic material deformation (*26*). This method incorporates constraints such as distance and strain, enabling the realistic representation of anisotropic growth processes observed in the root. This approach is particularly well-suited for capturing the directionally biased expansion of tissues during root development (*59*).

Boundary conditions

The meristematic zone, characterized by high cell proliferation, was aligned with the lateral root cap (*60*–*62*). The TZ was defined from the cusp of the last lateral root cap cell and extended shootward into the root mesh. The uppermost vertices of the root mesh were fixed to represent attachment to the differentiation zone (not modeled) and, by extension, the rest of the plant. All other mesh vertices, independent of zone, were unconstrained and updated according to the PBD engine. Wall stiffness was modulated by local QUA2 levels.

Biochemical processes

The biochemical layer of the model includes description of QUA2 protein expression by ordinary differential equations and is solved numerically using an explicit Euler scheme. To ensure stability and accuracy, a small time step is used (typically $\Delta t = 0.01$). The production of QUA2 protein is modeled in specific regions of the tissue, which are experimentally tracked and vary depending on the scenario (e.g., TZ). The dynamics of QUA2 protein production are governed by the following Ordinary Differential Equation (ODE)

$$\frac{d\mathrm{QUA2}}{dt} = b_{\mathrm{QUA}} - d_{\mathrm{QUA}} \cdot \mathrm{QUA2}$$

where QUA2 is a mean QUA2 protein concentration in the cell; b_{QUA} is a basal production rate; d_{QUA} is the QUA2 degradation rate.

The QUA2 level controls the cell wall relaxation parameter for PBD following an exponential decay relationship

$$kE_{\mathrm{wall}} = kE_{\mathrm{wall}} \cdot e^{(-K_{\mathrm{QUA}} \cdot \mathrm{QUA})}$$

where kE_{wall} is the basal stiffness of the cell wall; K_{QUA} is quasimodo relaxation (stiffness coefficient; QUA2 is the protein concentration inside the cell).

QUA2 expression pattern and mutant scenarios

In WT-like simulation, b_{QUA} is highly expressed in epidermal tissues (as most QUA2 is produces in epidermis) and exponentially decay toward the meristem zone (MZ), according to formula $b_{\mathrm{QUA}} = b_{\mathrm{QUA}} * (2/\{1/\exp[-0.04 * (\mathrm{cell\_pos} - \mathrm{MZ})]\})$ $b_{QUA} = b_{QUA} * 2/[1 + e^{-0.04 * (cell\_pos - MZ)}]$ to mimic the pattern observed in planta. As QUA2 expression is observed in the internal tissues of the root—at much lower levels—in WT-like simulation, we set a lower rate of QUA2 production in all radial tissues between the epidermis, respecting the same exponential decay toward the MZ mentioned.

The qua2 mutants were simulated by setting b_{QUA} to zero everywhere. QUA2 TZ overexpression was simulated by increasing b_{QUA} in all root tissues by 0.1.

Parameters were sampled using hundreds of parallel simulations on the supercomputing cluster to identify optimal values that do not introduce growth artifacts and mimic closely the WT-like root growth to allow base calibration to introduce mutants. Parameters are listed in table S7.

Supplementary Materials

The PDF file includes:

Supplementary Text
Figs. S1 to S4
Tables S1 to S7
Legends for movies S1 to S6

Other Supplementary Material for this manuscript includes the following:

Movies S1 to S6

REFERENCES

1. L. Dolan, K. Janmaat, V. Willemsen, P. Linstead, S. Poethig, K. Roberts, B. Scheres, Cellular organisation of the Arabidopsis thaliana root. *Development* **119**, 71–84 (1993).
2. N. Svolacchia, E. Salvi, S. Sabatini, Arabidopsis primary root growth: Let it grow, can't hold it back anymore! *Curr. Opin. Plant Biol.* **57**, 133–141 (2020).
3. E. Salvi, R. Di Mambro, S. Sabatini, Dissecting mechanisms in root growth from the transition zone perspective. *J. Exp. Bot.* **71**, 2390–2396 (2020).
4. R. Dello Ioio, F. S. Linhares, E. Scacchi, E. Casamitjana-Martinez, R. Heidstra, P. Costantino, S. Sabatini, R. Dello Ioio, F. S. Linhares, E. Scacchi, E. Casamitjana-Martinez, R. Heidstra, P. Costantino, S. Sabatini, Cytokinins determine arabidopsis root-meristem size by controlling cell differentiation. *Curr. Biol.* **17**, 678–682 (2007).
5. E. Salvi, J. P. Rutten, R. Di Mambro, L. Polverari, V. Licursi, R. Negri, R. Dello Ioio, S. Sabatini, K. Ten Tusscher, A self-organized PLT/Auxin/ARR-B network controls the dynamics of root zonation development in Arabidopsis thaliana. *Dev. Cell* **53**, 431–443.e23 (2020).
6. R. Dello Ioio, K. Nakamura, L. Moubayidin, S. Perilli, M. Taniguchi, M. T. Morita, T. Aoyama, P. Costantino, S. Sabatini, A genetic framework for the control of cell division and differentiation in the root meristem. *Science* **322**, 1380–1384 (2008).
7. R. Di Mambro, M. De Ruvo, E. Pacifici, E. Salvi, R. Sozzani, P. N. Benfey, W. Busch, O. Novak, K. Ljung, L. Di Paola, A. F. M. M. Marée, P. Costantino, V. A. Grieneisen, S. Sabatini, Auxin minimum triggers the developmental switch from cell division to cell differentiation in the Arabidopsis root. *Proc. Natl. Acad. Sci. U.S.A.* **114**, E7641–E7649 (2017).
8. M. Shtin, L. Polverari, N. Svolacchia, G. Bertolotti, S. J. Unterholzner, R. Di Mambro, P. Costantino, R. Dello Ioio, S. Sabatini, The mutual inhibition between PLETHORAs and ARABIDOPSIS RESPONSE REGULATORs controls root zonation. *Plant Cell Physiol.* **64**, 317–324 (2023).
9. E. Pacifici, R. Di Mambro, R. Dello Ioio, P. Costantino, S. Sabatini, Acidic cell elongation drives cell differentiation in the *Arabidopsis* root. *EMBO J.* **37**, e99134 (2018).
10. S. Liu, S. Strauss, M. Adibi, G. Mosca, S. Yoshida, R. Dello Ioio, A. Runions, T. G. Andersen, G. Grossmann, P. Huijser, R. S. Smith, M. Tsiantis, Cytokinin promotes growth cessation in the Arabidopsis root. *Curr. Biol.* **32**, 1974–1985.e3 (2022).
11. M. Fagard, T. Desnos, T. Desprez, F. Goubet, G. Refregier, G. Mouille, M. McCann, C. Rayon, S. Vernhettes, H. Höfte, Procuste1 encodes a cellulose synthase required for normal cell elongation specifically in roots and dark-grown hypocotyls of arabidopsis. *Plant Cell* **12**, 2409–2423 (2000).
12. L. Dash, S. Swaminathan, J. Šimura, C. L. P. Gonzales, C. Montes, N. Solanki, L. Mejia, K. Ljung, O. A. Zabotina, D. R. Kelley, Changes in cell wall composition due to a pectin biosynthesis enzyme GAUT10 impact root growth. *Plant Physiol.* **193**, 2480–2497 (2023).

13. L. M. Di Fino, M. S. Anjam, M. Besten, A. Mentzelopoulou, V. Papadakis, N. Zahid, L. A. Baez, N. Trozzi, M. Majda, X. Ma, T. Hamann, J. Sprakel, P. N. Moschou, R. S. Smith, P. Marhavý, Cellular damage triggers mechano-chemical control of cell wall dynamics and patterned cell divisions in plant healing. *Dev. Cell* **60**, 1411–1422.e6 (2025).
14. O. Hamant, M. G. Heisler, H. Jönsson, P. Krupinski, M. Uyttewaal, P. Bokov, F. Corson, P. Sahlin, A. Boudaoud, E. M. Meyerowitz, Y. Couder, J. Traas, Developmental patterning by mechanical signals in Arabidopsis. *Science* **322**, 1650–1655 (2008).
15. Y. Pu, J. W. Walley, Z. Shen, M. G. Lang, S. P. Briggs, M. Estelle, D. R. Kelley, Quantitative early auxin root proteomics identifies GAUT10, a galacturonosyltransferase, as a novel regulator of root meristem maintenance. *Mol. Cell. Proteomics* **18**, 1157–1170 (2019).
16. D. J. Cosgrove, Re-constructing our models of cellulose and primary cell wall assembly. *Curr. Opin. Plant Biol.* **22**, 122–131 (2014).
17. D. M. Harris, K. Corbin, T. Wang, R. Gutierrez, A. L. Bertolo, C. Petti, D. M. Smilgies, J. M. Estevez, D. Bonetta, B. R. Urbanowicz, D. W. Ehrhardt, C. R. Somerville, J. K. C. Rose, M. Hong, S. DeBolt, Cellulose microfibril crystallinity is reduced by mutating C-terminal transmembrane region residues CESA1 A903V and CESA3 T942I of cellulose synthase. *Proc. Natl. Acad. Sci. U.S.A.* **109**, 4098–4103 (2012).
18. K. H. Caffall, S. Pattathil, S. E. Phillips, M. G. Hahn, D. Mohnen, Arabidopsis thaliana T-DNA mutants implicate GAUT genes in the biosynthesis of pectin and xylan in cell walls and seed testa. *Mol. Plant* **2**, 1000–1014 (2009).
19. G. Mouille, M. C. Ralet, C. Cavelier, C. Eland, D. Effroy, K. Hématy, L. McCartney, H. N. Truong, V. Gaudon, J. F. Thibault, A. Marchant, H. Höfte, Homogalacturonan synthesis in Arabidopsis thaliana requires a Golgi-localized protein with a putative methyltransferase domain. *Plant J.* **50**, 605–614 (2007).
20. J. Du, A. Kirui, S. Huang, L. Wang, W. J. Barnes, S. N. Kiemle, Y. Zheng, Y. Rui, M. Ruan, S. Qi, S. H. Kim, T. Wang, D. J. Cosgrove, C. T. Anderson, C. Xiao, Mutations in the pectin methyltransferase QUASIMODO2 influence cellulose biosynthesis and wall integrity in Arabidopsis. *Plant Cell* **32**, 3576–3597 (2020).
21. J. Boruc, E. Mylle, M. Duda, R. De Clercq, S. Rombauts, D. Geelen, P. Hilson, D. Inzé, D. Van Damme, E. Russinova, Systematic localization of the arabidopsis core cell cycle proteins reveals novel cell division complexes. *Plant Physiol.* **152**, 553–565 (2010).
22. P. Bouvet, C. Bevilacqua, Y. Ambekar, G. Antonacci, J. Au, S. Caponi, S. Chagnon-Lessard, J. Czarske, T. Dehoux, D. Fioretto, Y. Fu, J. Guck, T. Hamann, D. Heinemann, T. Jähnke, H. Jean-Ruel, I. Kabakova, K. Koski, N. Koukourakis, D. Krause, S. La Cavera, T. Landes, J. Li, H. Mahmodi, J. Margueritat, M. Mattarelli, M. Monaghan, D. R. Overby, F. Perez-Cota, E. Pontecorvo, R. Prevedel, G. Ruocco, J. Sandercock, G. Scarcelli, F. Scarponi, C. Testi, P. Török, L. Vovard, W. J. Weninger, V. Yakovlev, S. H. Yun, J. Zhang, F. Palombo, A. Bilenca, K. Elsayad, Consensus statement on Brillouin light scattering microscopy of biological materials. *Nat. Photonics* **19**, 681–691 (2025).
23. C. Handler, C. Testi, G. Scarcelli, Advantages of integrating Brillouin microscopy in multimodal mechanical mapping of cells and tissues. *Curr. Opin. Cell Biol.* **88**, 102341 (2024).
24. J. Zhang, G. Scarcelli, Mapping mechanical properties of biological materials via an add-on Brillouin module to confocal microscopes. *Nat. Protoc.* **16**, 1251–1275 (2021).
25. R. Prevedel, A. Diz-Muñoz, G. Ruocco, G. Antonacci, Brillouin microscopy: An emerging tool for mechanobiology. *Nat. Methods* **16**, 969–977 (2019).
26. M. Marconi, M. Gallemi, E. Benková, K. Wabnik, A coupled mechano-biochemical model for cell polarity guided anisotropic root growth. *eLife* **10**, e72132 (2021).
27. W. Decaestecker, R. A. Buono, M. L. Pfeiffer, N. Vangheluwe, J. Jourquin, M. Karimi, G. van Isterdael, T. Beeckman, M. K. Nowack, T. B. Jacobs, CRISPR-Tsko: A technique for efficient mutagenesis in specific cell types, tissues, or organs in Arabidopsis[open]. *Plant Cell* **31**, 2868–2887 (2019).
28. D. W. Thompson, *On Growth and Form*, J. T. Bonner, Ed. (Cambridge Univ. Press, 1992); https://doi.org/10.1017/cbo9781107325852.
29. P. B. Green, Mechanism for plant cellular morphogenesis. *Science* **138**, 1404–1405 (1962).
30. P. M. Lintilhac, Differentiation, organogenesis, and the tectonics of cell wall orientation. II. Separation of stresses in a two-dimensional model. *Am. J. Bot.* **61**, 135 (1974).
31. L. V. Beloussov, Mechanically based generative laws of morphogenesis. *Phys. Biol.* **5**, 015009 (2008).
32. K. J. Niklas, H.-C. Spatz, *Plant Physics* (University of Chicago Press, 2012).
33. T. Mammoto, A. Mammoto, D. E. Ingber, Mechanobiology and developmental control. *Annu. Rev. Cell Dev. Biol.* **29**, 27–61 (2013).
34. C. Jiang, A. Centonze, Y. Song, A. Chrisnandy, E. Tika, S. Rezakhani, Z. Zahedi, G. Bouvencourt, C. Dubois, A. Van Keymeulen, M. Lütolf, A. Sifrim, C. Blanpain, Collagen signaling and matrix stiffness regulate multipotency in glandular epithelial stem cells in mice. *Nat. Commun.* **15**, 10482 (2024).
35. D. Wirtz, K. Konstantopoulos, P. C. Searson, The physics of cancer: The role of physical interactions and mechanical forces in metastasis. *Nat. Rev. Cancer* **11**, 512–522 (2011).
36. Q. Liu, Q. Luo, Y. Ju, G. Song, Role of the mechanical microenvironment in cancer development and progression. *Cancer Biol. Med.* **17**, 282–292 (2020).
37. R. K. Jain, J. D. Martin, T. Stylianopoulos, The role of mechanical forces in tumor growth and therapy. *Annu. Rev. Biomed. Eng.* **16**, 321–346 (2014).
38. E. Zatulovskiy, S. Zhang, D. F. Berenson, B. R. Topacio, J. M. Skotheim, Cell growth dilutes the cell cycle inhibitor Rb to trigger cell division. *Science* **369**, 466–471 (2020).
39. J. J. Turner, J. C. Ewald, J. M. Skotheim, Cell size control in yeast. *Curr. Biol.* **22**, R350–R359 (2012).
40. E. Benková, M. G. Ivanchenko, J. Friml, S. Shishkova, J. G. Dubrovsky, A morphogenetic trigger: Is there an emerging concept in plant developmental biology? *Trends Plant Sci.* **14**, 189–193 (2009).
41. C. Galinha, H. Hofhuis, M. Luijten, V. Willemsen, I. Blilou, R. Heidstra, B. Scheres, PLETHORA proteins as dose-dependent master regulators of Arabidopsis root development. *Nature* **449**, 1053–1057 (2007).
42. M. Aida, D. Beis, R. Heidstra, V. Willemsen, I. Blilou, C. Galinha, L. Nussaume, Y. S. Noh, R. Amasino, B. Scheres, The PLETHORA genes mediate patterning of the Arabidopsis root stem cell niche. *Cell* **119**, 109–120 (2004).
43. M. M. Neff, J. D. Neff, J. Chory, A. E. Pepper, dCAPS, a simple technique for the genetic analysis of single nucleotide polymorphisms: Experimental applications in Arabidopsis thaliana genetics. *Plant J.* **14**, 387–392 (1998).
44. R. Di Mambro, S. Sabatini, "Developmental analysis of Arabidopsis root meristem," in *Methods in Molecular Biology* (Humana Press Inc., 2018), vol. 1761, pp. 33–45; https://link.springer.com/protocol/10.1007/978-1-4939-7747-5_3.
45. M. Stemmer, T. Thumberger, M. Del Sol Keyer, J. Wittbrodt, J. L. Mateo, CCTop: An intuitive, flexible and reliable CRISPR/Cas9 target prediction tool. *PLOS ONE* **10**, e0124633 (2015).
46. M. Labuhn, F. F. Adams, M. Ng, S. Knoess, A. Schambach, E. M. Charpentier, A. Schwarzer, J. L. Mateo, J. H. Klusmann, D. Heckl, Refined sgRNA efficacy prediction improves largeand small-scale CRISPR-Cas9 applications. *Nucleic Acids Res.* **46**, 1375–1385 (2018).
47. M. M. Marquès-Bueno, A. K. Morao, A. Cayrel, M. P. Platre, M. Barberon, E. Caillieux, V. Colot, Y. Jaillais, F. Roudier, G. Vert, A versatile Multisite Gateway-compatible promoter and transgenic line collection for cell type-specific functional genomics in Arabidopsis. *Plant J.* **85**, 320–333 (2016).
48. N. Gigli-Bisceglia, T. Engelsdorf, M. Strnad, L. Vaahtera, G. A. Khan, A. Jamoune, L. Alipanah, O. Novák, S. Persson, J. Hejatko, T. Hamann, Cell wall integrity modulates arabidopsis thaliana cell cycle gene expression in a cytokinin-and nitrate reductase-dependent manner. *Development* **145**, dev166678 (2018).
49. I. Rauschert, J. C. Benech, M. Sainz, O. Borsani, M. Sotelo-Silveira, Atomic force microscopy to study the physical properties of epidermal cells of live *Arabidopsis* roots. *J. Vis. Exp.* **2022**, e63533 (2022).
50. M. B. Cuadrado-Pedetti, I. Rauschert, M. M. Sainz, V. Amorim-Silva, M. A. Botella, O. Borsani, M. Sotelo-Silveira, The Arabidopsis TETRATRICOPEPTIDE THIOREDOXIN-LIKE 1 gene is involved in anisotropic root growth during osmotic stress adaptation. *Genes (Basel)* **12**, 236 (2021).
51. L. Sirghi, J. Ponti, F. Broggi, F. Rossi, Probing elasticity and adhesion of live cells by atomic force microscopy indentation. *Eur. Biophys. J.* **37**, 935–945 (2008).
52. L. Martinez-Vidal, C. Testi, E. Pontecorvo, F. Pederzoli, E. Alchera, I. Locatelli, C. Venegoni, A. Spinelli, R. Lucianò, A. Salonia, A. Podestà, G. Ruocco, M. Alfano, Progressive alteration of murine bladder elasticity in actinic cystitis detected by Brillouin microscopy. *Sci. Rep.* **14**, 484 (2024).
53. C. Bevilacqua, J. M. Gomez, U. M. Fiuza, C. J. Chan, L. Wang, S. Hambura, M. Eguren, J. Ellenberg, A. Diz-Muñoz, M. Leptin, R. Prevedel, High-resolution line-scan Brillouin microscopy for live imaging of mechanical properties during embryo development. *Nat. Methods* **20**, 755–760 (2023).
54. I. Kabakova, J. Zhang, Y. Xiang, S. Caponi, A. Bilenca, J. Guck, G. Scarcelli, Brillouin microscopy. *Nat. Rev. Methods Prim.* **4**, 8 (2024).
55. H. Keshmiri, D. Cikes, M. Samalova, L. Schindler, L. M. Appel, M. Urbanek, I. Yudushkin, D. Slade, W. J. Weninger, A. Peaucelle, J. Penninger, K. Elsayad, Brillouin light scattering anisotropy microscopy for imaging the viscoelastic anisotropy in living cells. *Nat. Photonics* **18**, 276–285 (2024).
56. K. Elsayad, S. Werner, M. Gallemí, J. Kong, E. R. S. Guajardo, L. Zhang, Y. Jaillais, T. Greb, Y. Belkhadir, Mapping the subcellular mechanical properties of live cells in tissues with fluorescence emission-Brillouin imaging. *Sci. Signal.* **9**, rs5 (2016).
57. P. Barbier de Reuille, A.-L. Routier-Kierzkowska, D. Kierzkowski, G. W. Bassel, T. Schüpbach, G. Tauriello, N. Bajpai, S. Strauss, A. Weber, A. Kiss, A. Burian, H. Hofhuis, A. Sapala, M. Lipowczan, M. B. Heimlicher, S. Robinson, E. M. Bayer, K. Basler, P. Koumoutsakos, A. H. Roeder, T. Aegerter-Wilmsen, N. Nakayama, M. Tsiantis, A. Hay, D. Kwiatkowska, I. Xenarios, C. Kuhlemeier, R. S. Smith, MorphoGraphX: A platform for quantifying morphogenesis in 4D. *eLife* **4**, 05864 (2015).
58. V. Capasso, M. Gromov, A. Harel-Bellan, N. Morozova, L. L. Pritchard, Pattern formation in morphogenesis: Problems and mathematical issues (2013); https://doi.org/10.1007/978-3-642-20164-6.
59. M. Müller, B. Heidelberger, M. Hennix, J. Ratcliff, Position based dynamics. *J. Vis. Commun. Image Represent.* **18**, 109–118 (2007).
60. M. P. Levesque, T. Vernoux, W. Busch, H. Cui, J. Y. Wang, I. Blilou, H. Hassan, K. Nakajima, N. Matsumoto, J. U. Lohmann, B. Scheres, P. N. Benfey, Whole-genome analysis of the SHORT-ROOT developmental pathway in Arabidopsis. *PLoS Biol.* **4**, e143 (2006).

61. R. Di Mambro, S. Sabatini, R. Dello Ioio, Patterning the axes: A lesson from the root. *Plants* **8**, 1–13 (2019).
62. A. S. Iyer-Pascuzzi, P. N. Benfey, Transcriptional networks in root cell fate specification. *Biochim. Biophys. Acta* **1789**, 315–325 (2009).

Acknowledgments: We thank D. Scintu, F. Cazzaniga, M. Shtin, S. Amati, C. A. De Filippo, S. J. Unterholzner, G. S. Montanha, E. Di Pietro, and M. De Vivo for helpful discussions. We also thank F. Lucantoni for technical support and the Plataforma de Microscopía de Fuerza Atómica at the Instituto de Investigaciones Biológicas Clemente Estable for support. **Funding:** This work was supported by the National Science Foundation grant PRFB 2109634 (LRL), Ministerio de Ciencia Innovacion y Universidades of Spain grant PID2021-122158NB-I00 and CNS2023-143915 (K.W.), Programa de Atraccion de Talento 2017 (Comunidad de Madrid 2021-5 A/BIO-20952) (K.W.), and Severo Ochoa (SO) Program for Centres of Excellence in R&D from the Agencia Estatal de Investigación of Spain grant CEX2020-000999-S (2022 to 2025) to the CBGP (K.W.). This study was carried out within the Agritech National Research Center and received funding from the European Union Next-GenerationEU [PIANO NAZIONALE DI RIPRESA E RESILIENZA (PNRR)–MISSIONE 4 COMPONENTE 2, INVESTIMENTO 1.4–D.D. 1032 17 June 2022, CN00000022] (S.S.), Ministero dell'Università e Ricerca (grant number PRIN2022-2022NZ7M3W-PRIN2022), and The Giovanni Armenise FY21-22 CDA Mid-Career grant. R.D.I., N.S., and G.B. were supported by the PRINN2022 grant and Ministero dell'Università e Ricerca (grant number 20229LHY5L-PRIN2022). R.D.M. and A.T. were supported by the PRINN2022 grant and Ministero dell'Università e Ricerca (grant number PRIN2022-20229K8ZWF). **Author contributions:** Conceptualization: S.S. Methodology: S.S., K.W., N.S., R.D.I., R.D.M., M.M., J.E.P., M.S.-S., C.T., and G.R. Investigation: N.S., F.V., M.D.N., A.T., G.B., E.S., K.W., M.M., J.E.P., M.S.-S., C.T., and G.R. Resources: S.S., R.D.I., and R.D.M. Software: K.W., M.M., and J.E.P. Visualization: K.W., M.M., J.E.P., and N.S. Supervision: S.S., R.D.I., and R.D.M. Writing—original draft: S.S., K.W., and N.S. Writing—review and editing: All authors. **Competing interests:** The authors declare that they have no competing interests. **Data and materials availability:** All data and code needed to evaluate and reproduce the results in the paper are present in the paper and/or the Supplementary Materials.

Submitted 23 July 2025
Accepted 17 November 2025
Published 19 December 2025
10.1126/sciadv.aea8647